$$\begin{bmatrix}\Delta u_d\\ \Delta u_q\end{bmatrix}=\begin{bmatrix}K_d+Q_d(2\theta)\\ K_q+Q_q(2\theta)\end{bmatrix}=\frac{U_s}{2}\times \left\{\begin{matrix}(k_1\cos\delta_1+k_3\cos\delta_2)+\left[k_2\cos(2\theta+\delta_1)+k_4\cos(2\theta+\delta_2)\right]\\ (k_1\sin\delta_1+k_3\sin\delta_2)-\left[k_2\sin(2\theta+\delta_1)+k_4\sin(2\theta+\delta_2)\right]\end{matrix}\right\} \tag{12}$$

$$\begin{bmatrix}\Delta u_x\\ \Delta u_y\end{bmatrix}=\begin{bmatrix}Q_x(\theta)\\ Q_y(\theta)\end{bmatrix}=\frac{U_s}{2}\times \left\{\begin{matrix}(k_1+k_2)\cos(\theta+\delta_1)-(k_3+k_4)\cos(\theta+\delta_2)\\ -(k_1-k_2)\sin(\theta+\delta_1)+(k_3-k_4)\sin(\theta+\delta_2)\end{matrix}\right\} \tag{13}$$

Furthermore, the equivalent circuits of a dual three-phase PMSM considering asymmetry can be obtained in Fig. 3.

From the equivalent circuits in Fig.3, it can be seen that the asymmetry causes an additional fundamental current component on the *x-y* subspace, and a DC component and second order component on the *d-q* subspace. The asymmetric current components on the *d-q* subspace cause torque ripple, and the asymmetric current components on the *x-y* subspace cause additional copper loss. A mitigation strategy for asymmetric currents will be presented in section V.

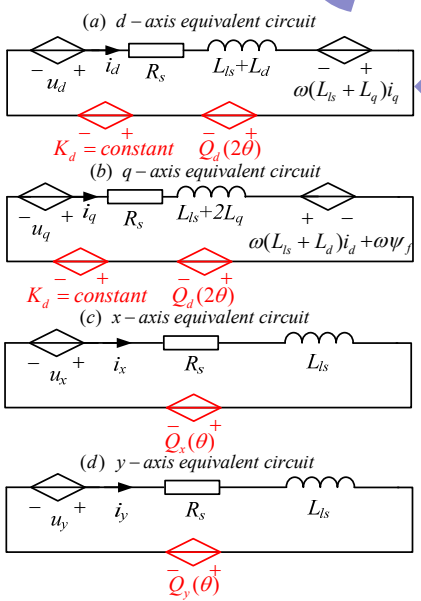

Fig. 3. Equivalent circuits of a dual three-phase PMSM under the VSD frame considering asymmetry.

III. DT-SVM FOR NPC-3L SIX-PHASE INVERTERS

The proposed dual three-phase space vector modulation (DT-SVM) strategy for NPC-3L six-phase inverters actually comprises two sets of three-phase SVM modules. The voltage vectors of the two sets of three-phase inverters can be defined as follows:

$$\boldsymbol{U}_1=\frac{2}{3}(u_{AM}e^{j0}+u_{CM}e^{j\frac{2\pi}{3}}+u_{EM}e^{j\frac{4\pi}{3}}) \tag{14}$$

$$\boldsymbol{U}_2=\frac{2}{3}(u_{BM}e^{j\frac{\pi}{6}}+u_{DM}e^{j\frac{5\pi}{6}}+u_{FM}e^{j\frac{3\pi}{2}}) \tag{15}$$

where $u_{xM}=S_xU_{dc}/2$（x=A~F）is the pole voltage of the x phase and S_x (–1, 0, 1,) are the level states of the x phase. The states of S_x can also be expressed by the symbols N, O and P, respectively. Accordingly, a vector diagram of the polar voltage for NPC-3L six-phase inverters is presented in Fig. 4(a). Furthermore, a vector diagram of the line voltage is presented in Fig. 4(b), where the symbols "+" and "–" represent the voltage values U_{dc} and $-U_{dc}$, respectively. As shown in Fig. 4, the black lines correspond to the voltage vector diagram of the ACE-phase inverter and the blue lines correspond to the voltage vector diagram of the BDF-phase inverter. Both of the dual vector diagrams comprise 27 voltage vectors, which consist of 19 effective vectors and 8 redundant vectors. The 19 effective vectors divide each of the dual vector diagrams on 6 large sectors. Each of the large sectors is further divided into 4 subsectors. In term of the differences in vector lengths, the total 27 vectors can be classified into 4 categories containing large vectors, medium vectors, small vectors and zero vectors, as shown in Table I.

TABLE I
VOLTAGE VECTORS CATEGORIES FOR THE NPC-3L SIX-PHASE INVERTER OF THE DT-SVM STRATEGY

Classes	Number	Length	Vectors
Large vectors	6	$2U_{dc}/3$	PNN/PPN/NPN/ NPP/NNP/PNP/
Medium vectors	6	$\sqrt{3}U_{dc}/3$	PON/OPN/NPO/ NOP/ONP/PNO
Small vectors	12	$U_{dc}/3$	POO/ONN/PPO/ OON/OPO/NON/ OPP/NOO/OOP/ NNO/POP/ONO/
Zero vectors	3	0	OOO/PPP/NNN

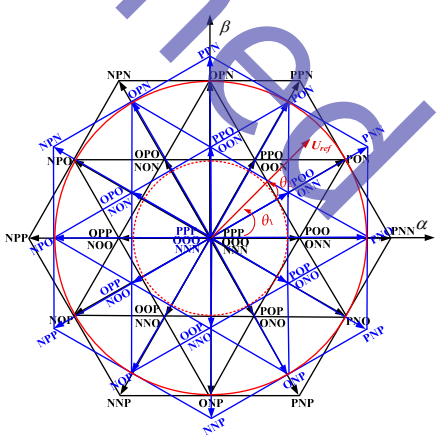

(a)

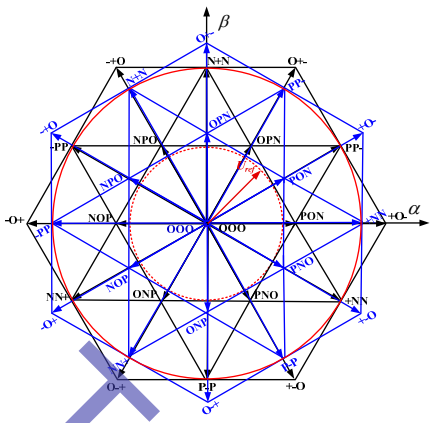

(b)

Fig. 4. Voltage vectors diagrams for the NPC-3L six-phase inverters of the DT-SVM strategy: (a) pole voltage vectors diagram; (b) line voltage vector diagram.

In Fig. 4, it is observed that the DT-SVM vector diagram consist of two sets of NPC-3L three-phase vectors diagrams shifted by 30 degrees. The modulation processes of the two sets of three-phase vectors diagrams are similar. When the reference voltage $\boldsymbol{U}_{ref}$ on the α-β subspace is determined, the reference voltages for the modulation in two sets are obtained as shown in Eq. (16):

$$\begin{cases} \boldsymbol{U}_{1ref} = U_{ref} \angle \theta \\ \boldsymbol{U}_{2ref} = U_{ref} \angle (\theta - 30^\circ) \end{cases} \tag{16}$$

where U_{ref} is the amplitude of the reference voltage vector in the α-β subspace, $\boldsymbol{U}_{1ref}$ is the reference voltage vector in the vector diagram of the ACE-phase inverter, and $\boldsymbol{U}_{2ref}$ is the reference voltage vector in the vector diagram of the BDF-phase inverter.

For example, in sector 1 of the ACE-phase vector diagram, the subsectors of sector 1 are referred to as A, B, C and D. The nearest three vectors (NTV) around the reference voltage vector vertex are selected for synthesizing the reference voltage vector $\boldsymbol{U}_{ref}$. As shown by the location of the reference vector in Fig.5, the NTV are $\boldsymbol{U}_2$, $\boldsymbol{U}_4$ and $\boldsymbol{U}_5$.

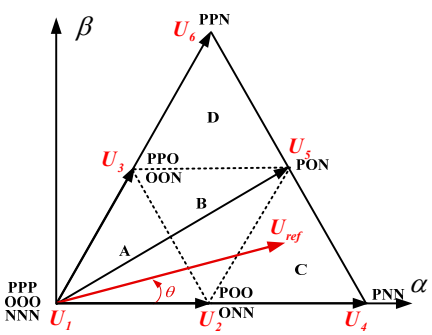

Fig. 5. Sector I of the vector diagram in the ACE-phase inverter.

Consequently, the voltage utilization factor is defined as $H = U_{ref} / U_{dc}$ and the modulation depth is defined to be $M = \sqrt{3} U_{ref} / U_{dc}$. According to the volt-second balance principle in Eq. (17), the vectors operation time of the NTV for the synthesizing reference voltage vector can be obtained as (18).

$$\begin{cases} \boldsymbol{U}_2 T_{U2} + \boldsymbol{U}_4 T_{U4} + \boldsymbol{U}_5 T_{U5} = \boldsymbol{U}_{1ref} T_s \\ T_{U2} + T_{U4} + T_{U5} = T_s \end{cases} \tag{17}$$

$$\begin{bmatrix} T_{U2} \\ T_{U4} \\ T_{U5} \end{bmatrix} = \begin{bmatrix} 2T_s - 2\sqrt{3} H T_s \sin(\theta + 60^\circ) \\ 2\sqrt{3} H T_s \sin(60^\circ - \theta) - T_s \\ 2\sqrt{3} H T_s \sin(\theta) \end{bmatrix} \tag{18}$$

where T_{U2}, T_{U4} and T_{U5} are the vectors operation times of $\boldsymbol{U}_2$, $\boldsymbol{U}_4$ and $\boldsymbol{U}_5$, respectively, and T_s is the time of the switching period.

The 7-segment symmetric vector operation sequence is used, which takes full advantage of the redundant voltage vectors of the NTV. The 7-segment vector operation sequences in sector 1 are presented in Table II, where t_1=t_7=T_1/4, t_2=t_6=T_2/2, t_3=t_5=T_3/2 and t_4=T_1/2. In addition, T_1, T_2 and T_3 are the dwelling times of the selected voltage vectors.

TABLE II

7-SEGMENT VECTOR OPERATION SEQUENCES IN SECTOR 1

Time \ Subsectors	A	B	C	D
t_1	POO	POO	POO	PPO
t_2	OOO	PON	PON	PPN
t_3	OON	OON	PNN	PON
t_4	ONN	ONN	ONN	OON
t_5	OON	OON	PNN	PON
t_6	OOO	PON	PON	PPN
t_7	POO	POO	POO	PPO

The location judgment of the reference voltage vector consists of the judgment of the sector and the judgment of the subsector. The per unit value of the reference voltage vector is defined as $\boldsymbol{U}_{ref.pu} = \boldsymbol{U}_{ref} / U_{dc}$. In addition, $\boldsymbol{U}_{ref.pu}$ can be written in the polar coordinate form and the plural form as shown in Eq. (19). According to the range of θ, the sector number of the reference voltage vector can be easily obtained. The subsector number can be determined in term of the judgmental principle listed in Table III.

$$\begin{cases} \boldsymbol{U}_{ref.pu} = U_{ref.pu} \angle \theta \\ \boldsymbol{U}_{ref.pu} = U_{\alpha.pu} + j U_{\beta.pu} \end{cases} \tag{19}$$

TABLE III

JUDGMENTAL PRINCIPLE TO DETERMINE SUBSECTORS OF THE REFERENCE VOLTAGE VECTOR

Judgment principles	Subsectors
$\sqrt{3} U_{\alpha.pu} + U_{\beta.pu} < H / \sqrt{3}$	A
$\sqrt{3} U_{\alpha.pu} - U_{\beta.pu} \geq H / \sqrt{3}$	C

$U_{\beta.pu} \geq \sqrt{3}H/6$	D
Else	B

IV. DC Link Capacitors Voltage Balancing Control

The impacts of different vector categories for the middle voltage of DC link capacitors are different. The impacts of those vectors are summarized as: (1) large vectors and zero vectors have no effect on the mid-point voltage; (2) medium vectors cause fluctuations of the mid-point voltage, which cannot be controlled by a modulation strategy; (3) small vectors, appearing in pairs, have the opposite effects on the mid-point voltage [28]. For example, the positive small vector PPO has the trend of raising the mid-point voltage, and the negative small vector OON has the trend of lowering the mid-point voltage. Hence, the DC-link mid-point voltage can be balanced by dynamically adjusting the dwelling time of the redundant small vectors. The balancing factor λ is introduced to distribute the dwelling time of the redundant small vectors in Table II.

$$\begin{cases} t_1 = t_7 = (1+\lambda)T_1/4 \\ t_4 = (1-\lambda)T_1/2 \end{cases} \tag{20}$$

Thus, the factors resulting in fluctuations of the mid-point voltage can be concluded to be: (1) the modulation depth M, which mainly determines the dwelling time of the medium vectors and small vectors; (2) the loading current I, which determines the current value flowing on the mid-point of the DC link; (3) the loading power factor, pf, which determines the direction of the current flow on the mid-point of the DC link; (4) the upper and lower capacitor values C in the DC link; and (5) the balancing factor λ, which is the only adjusting factor for balancing the mid-point voltage in the DC link. Consequently, the voltage difference between the upper capacitor and lower capacitor in the DC link is expressed as follows.

$$\Delta U_c = \frac{I_{pu}}{C_{pu}} f(M, pf, \lambda) \tag{21}$$

where I_{pu} is the per unit value of the load current amplitude, and the rated value is 10A. C_{pu} is the per unit value of the DC link capacitors C, and the value is 1000 uF. Actually, the expression $f(M, pf, \lambda)$ is a highly nonlinear function, which is very difficult to express with a time-domain expression. Some research have studied the relationships between ΔU_c and M, and pf and λ. In [28], a new model in the *d-q* coordinate frame is proposed to describe the expression of the middle current with a complicated piecewise function, which indirectly reflects middle voltage of the DC link. In [29], the equivalent circuit of a NPC-3L inverter is modelled and the middle voltage expression is derived with the Laplace-domain. However, in engineering applications, these complicated expressions are seldom done by digital controllers like a DSP. In this paper, an effective method is proposed based on a numerical simulation. The expression Eq. (21) is discretised into several values by a numerical simulation with Matlab/Simulink, and they are saved in the memory of the controller. With allowable deviations of the middle voltage, the loading current I, the loading power factor pf and the modulation depth M, the appropriate balancing factor λ can be obtained by an interpolation approach based on the discrete values of Eq. (21). Fig.6 presents the interpolation fitting surface of Eq. (21).

As shown in Fig. 6, some valuable conclusions can be obtained to guide in the selection of an appropriate balancing factor λ for minimizing mid-point voltage fluctuations: (1) with the same balancing factor λ, a high modulation index benefits the balancing of the DC link mid-point voltage with a high power factor pf in the load. On the other hand, a low modulation index has a lower DC link mid-point voltage with a low power factor in the load. (2) For medium and low modulation indexes, an appropriate increase of the balancing factor λ can suppress mid-point voltage fluctuations. However, an excessive increasing of λ aggravates the mid-point voltage fluctuations. (3) For a high modulation index, the balancing factor λ loses controllability of the mid-point voltage in the DC link.

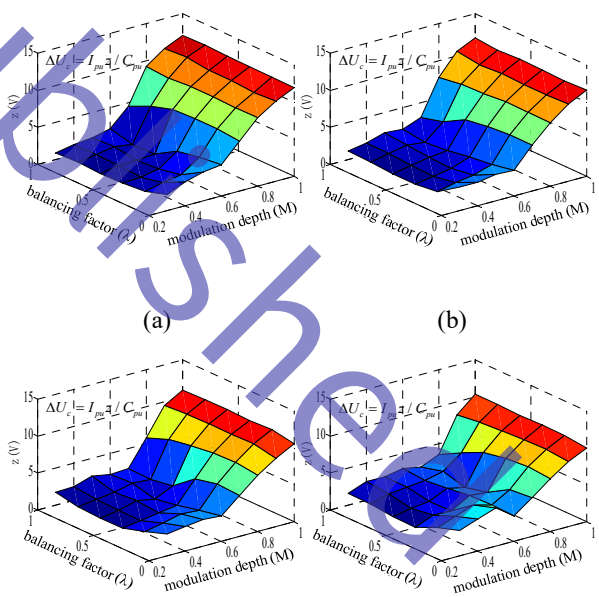

(a) (b) (c) (d)

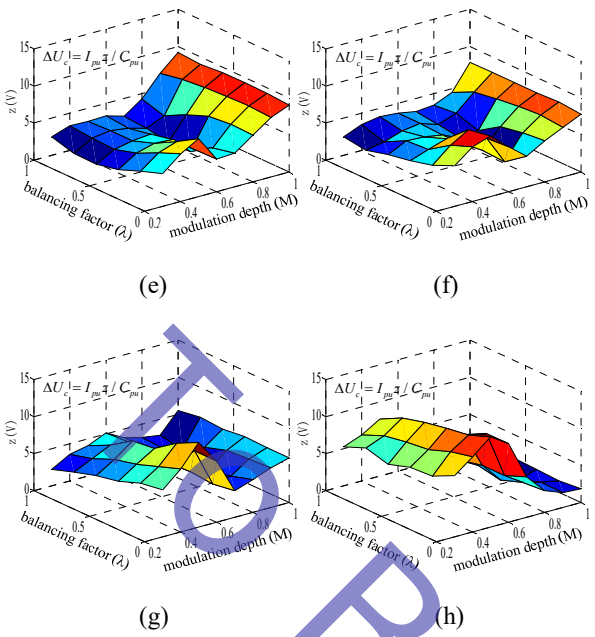

Fig. 6. Numerical fitting surface of the voltage difference between the upper capacitor and the lower capacitor: (a) load character pf=0.3; (b) load character pf=0.4; (c) load character pf=0.5; (d) load character pf=0.6; (e) load character pf=0.7; (f) load character pf=0.8; (g) load character pf=0.9; and (h) load character pf=1.0.

V. CONTROL SCHEME

Based on the aforementioned VSD model of a dual three-phase PMSM, the torque component can be controlled in the *d-q* subspace, and the asymmetric component can be suppressed in the *x-y* subspace. Furthermore, the modulation of reference voltage and balancing control of the mid-point voltage can be implemented by the DT-SVM strategy. Fig. 7 presents a block diagram of the vector control for NPC-3L six-phase inverter fed dual three-phase PMSM drives by considering asymmetric factors.

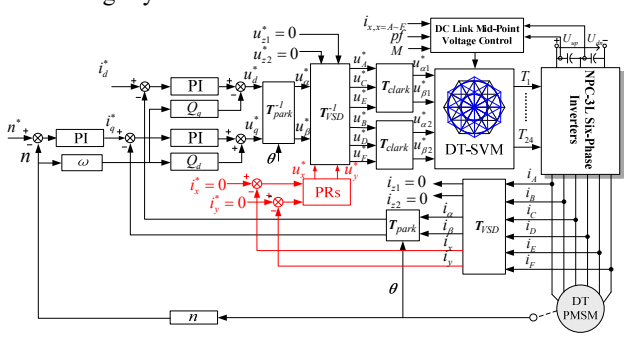

Fig. 7. Proposed control block diagram of NPC-3L six-phase inverter fed dual three-phase PMSM drives considering asymmetric factors.

As shown in Fig. 7, the outer speed controller generates the *q*-axis current reference, and the *d*-axis current reference is kept zero for the zero d-axis current (ZDC) operation. The inner current controller in the *d-q* subspace adopts PI control to generate the *d*-axis and *q*-axis voltage references, namely u_d^* and u_q^*. The feedforward compensation terms $Q_d = \omega(L_d + L_{ls})i_d + \omega\psi_f$ and $Q_q = \omega(L_q + L_{ls})i_q$ are added to the *q*-axis and *d*-axis current controllers for decoupling the interactions between the *d*-axis and *q*-axis. Thus, the dynamic performance of the drive system can be improved. The bandwidths of the *d*-axis and *q*-axis PI current controllers are designed slightly larger than twice the fundamental frequency (2ω). Therefore, the oscillating terms $Q(2\theta)$ in Fig. 3(a) and Fig. 3(b) can be effectively controlled. Then applying the transformation matrix $\boldsymbol{T}_{park}^{-1}$ to the voltage references vector $[u_d^*, u_q^*]^{\mathrm{T}}$, the voltage references u_α^* and u_β^* are obtained. $\boldsymbol{T}_{park}^{-1}$ is the inverse matrix of $\boldsymbol{T}_{park}$ in Eq. (6).

Meanwhile, the inner current controller in the *x-y* subspace adopts a proportional resonant (PR) controller for controlling the *x*-axis and *y*-axis currents to be zero. Then the voltage references u_x^* and u_y^* are obtained. The transfer function of the PR controllers in Fig.7 is given as follows:

$$G(s) = K_p + \frac{2K_r\omega_c s}{s^2 + 2\omega_c s + \omega^2} \tag{22}$$

where K_p and K_r are the proportional and resonant coefficients, respectively, ω is the fundamental frequency, and ω_c is the cut-off frequency, which is helpful for reducing the sensitivity to slight frequency oscillations of the fundamental frequency. A smaller ω_c makes the PR controllers more sensitive to frequency variations and lead to a slower transient response. The value of ω_c is chosen to be 0.02 times the fundamental frequency in this paper, which is based on the better experimental performance in Section VI. The z transformation makes it easier to execute Eq. (22) by a DSP, and the z transformation expression of Eq. (22) is presented as follows:

$$G(z) = K_p z^0 + \frac{2K_r\omega_c z^0 - 2K_r\omega_c e^{-\omega_c T}\left[\cos(\Delta\times T) + \frac{\omega_c}{\Delta}\sin(\Delta\times T)\right]z^{-1}}{1 - 2e^{-\omega_c T}\cos(\Delta\times T)z^{-1} + e^{-2\omega_c T}z^{-2}} \tag{23}$$

where $\Delta = \sqrt{\omega^2 - \omega_c^2}$, and T is the control period in the DSP.

Furthermore, by multiplying the inverse transformation of $\boldsymbol{T}_{VSD}$ to the voltage references vector $[u_\alpha^*, u_\beta^*, u_x^*, u_y^*, u_{z1}^* = 0, u_{z2}^* = 0]$, the voltage references on the natural frames, namely u_x (x=A~F) are obtained. Then with a Clark transform, the voltage references $u_{\alpha 1}^*$ and $u_{\beta 1}^*$ are provided for the first three-phase NPC-3L inverter, and the voltage references $u_{\alpha 2}^*$ and $u_{\beta 2}^*$ are provided for the second inverter. The Clark transform matrix $\boldsymbol{T}_{clark}$ is given in Eq. (24).

$$\boldsymbol{T}_{clark} = \frac{2}{3}\begin{bmatrix} 1 & -1/2 & -1/2 \\ 0 & \sqrt{3}/2 & -\sqrt{3}/2 \end{bmatrix} \tag{24}$$

The switching signals are generated with the modulation strategy in section III and the balancing factor λ in section IV.

VI. Experimental Verification

A laboratory experimental platform of a NPC-3L inverter fed dual three-phase PMSM drive is built to verify the validity of the presented analysis and control scheme considering asymmetric factors. The control part consists of a DSP (TMS-F28335) and a FPGA (Xinlix-Spartan6), which are used to implement the control algorithms and switching strategies, respectively. The power conversion circuit is constructed by IGBT models (F3L100R07W2E3-B11). A PM machine feeding the resistors is coupled to the tested dual three-phase PMSM machine for providing a load. The system parameters of the experiments are given in Table IV.

TABLE IV
Main Parameters in the Experiments

Name	Value
Pole pair number n_p	3
Stator resistance R_p	0.4 Ω
PM flux (peak) ψ_f	0.31 Wb
q-axis inductance L_q	8.71 mH
d-axis inductance L_d	5.68 mH
Experimental speed	550 rpm
DC voltage U_{dc}	115 V
Switching frequency	5 kHz
Balancing factor λ	0.9
Load type	Generator

Fig. 8 shows measured steady-state waveforms of dual three-phase PMSM drives without using closed-loop current control in the x-y subspace. Due to the inevitable differences in the parameters of the dual three-phase windings, the phase currents show slight difference in the waveforms of i_A and i_B as shown in Fig. 8(a). Thus, the unbalanced components cause a fundamental-frequency component with a peak value of about 0.4A in the x-y subspace as shown in Fig. 8(b). Fig. 9 shows the performance when a closed-loop current controller is added to the x-y subspace. As mentioned in section V, the closed-loop current controller can eliminate the fundamental current component in the x-y subspace in such a way that the asymmetry of the phase currents in the dual three-phase windings can be mitigated. Fig. 9(a) shows that the slight differences in the phase currents of dual the three-phase windings are effectively removed, and Fig. 9(b) shows that the fundamental current components in the x-y subspace are effectively eliminated. Furthermore, an additional 5mH inductor is connected to the B phase. Therefore, the asymmetry issue becomes aggravated. Fig. 9(c) and (d) verify that the proposed closed-loop current control in the x-y subspace are still effective in suppressing unbalanced phase currents by eliminating the current components in the x-y subspace.

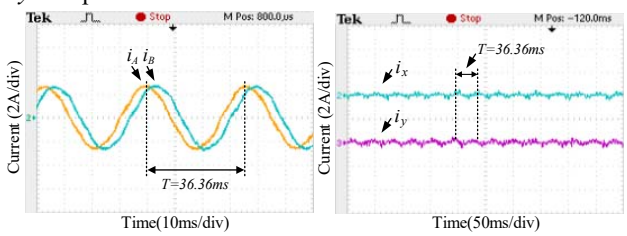

(a) (b)

Fig. 8. Measured steady-state waveforms with the open-loop control in the x-y subspace: (a) A-phase and B-phase currents; (b) phase current components in the x-y subspace.

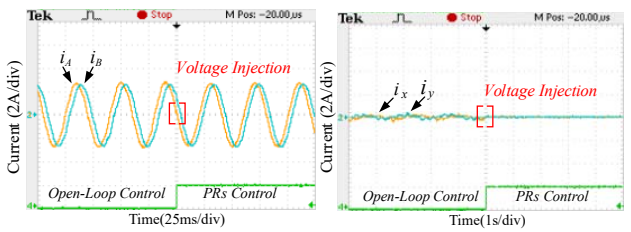

(a) (b)

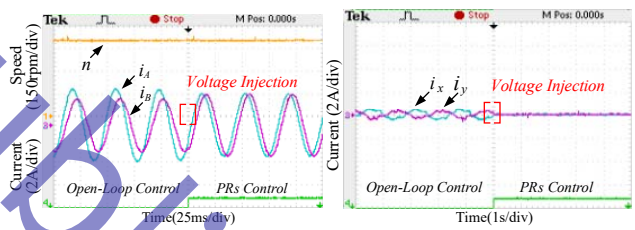

(c) (d)

Fig. 9. Measured transient performance of the proposed PR based controller in the x-y subspace: (a) phase A and phase B currents; (b) harmonic current components in the x-y subspace; (c) phase A and phase B currents while connecting a 5mH inductor to phase B; and (d) current components in the x-y subspace while connecting a 5mH inductor to phase B.

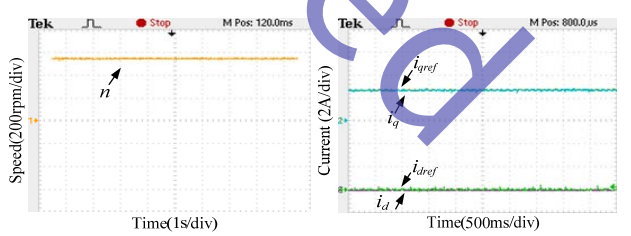

(a) (b)

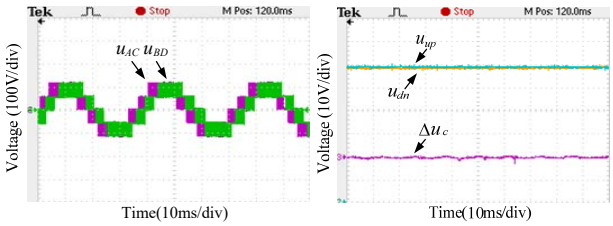

(c) (d)

Fig. 10. Measured steady-state waveforms of a dual three-phase PMSM drive with the proposed control scheme: (a) rotor speed; (b) *d-q* axis reference currents and measured currents, (c) line voltages (AC, BD); (d) DC capacitor voltages and the voltage difference between the upper and the lower capacitors.

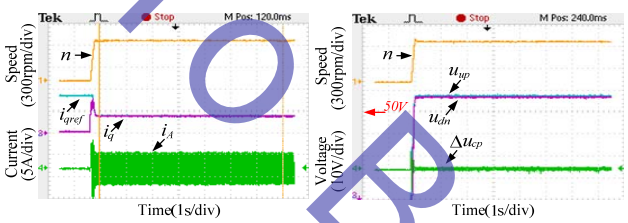

(a) (b)

Secondly, measured steady-state waveforms of a dual three-phase PMSM drive base on the proposed control diagram are presented in Fig. 10. The load torque is 7.46 Nm and the operation speed is stably controlled at 550 rpm as shown in Fig. 10(a). Fig. 10(b) shows measured steady-state waveforms of the *d-q* axis reference currents and measured currents. The actual currents can accurately track their reference values. The waveforms of the line-to-line voltages (AC, BD) present five-level states with a 30-degree shifted angle as shown in Fig. 10(c). Fig. 10(d) presents waveforms of the DC capacitor voltages and the mid-point voltage deviation in the DC link. This indicates that the difference between the upper and lower capacitor voltages is less than 5% U_{dc}.

Thirdly, the measured dynamic performance of the proposed control scheme for dual three-phase PMSM drives during the starting process is plotted as shown in Fig.11. The motor speed goes from 0 rpm to 550 rpm and the q-axis current tracks the reference current accurately and rapidly as shown in Fig. 11(a). The upper and lower capacitor voltages in the DC link are balanced well during the dynamic process as shown in Fig. 11(b). Furthermore, Fig. 12 shows the measured dynamic performance of the drive when the operation speed is changed, where the machine speed increases from -400 rpm to 400 rpm, and then decreases back to -400 rpm. As shown in Fig. 12(a), the measured q-axis current still tracks the reference current accurately and rapidly. The upper and lower capacitor voltages of the DC link are also balanced well in the dynamic process in Fig.12 (b). Fig. 14 shows the measured dynamic performance of the drive with a change in the load, where the torque is changed between 2.21 Nm and 7.46 Nm. In addition, the q-axis current can track the reference current accurately and rapidly in Fig. 13(a), and the DC link capacitor voltages are balanced well in Fig. 13(b).

Fig. 11. Measured transient performance of the drive of the proposed control scheme during the starting process: (a) rotor speed, q-axis current and phase-A current; (b) rotor speed, DC capacitor voltages and voltage difference between the upper and lower capacitors in the DC link.

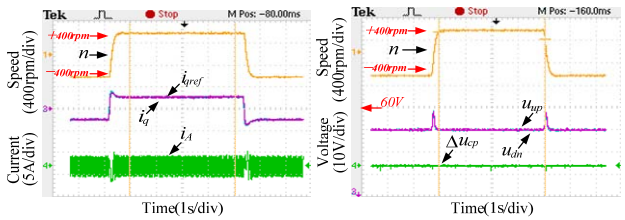

(a) (b)

Fig. 12. Measured dynamic performance of the drive of the proposed control scheme under change in speed: (a) rotor speed, q-axis current and phase-A current; (b) rotor speed, DC capacitor voltages and voltage difference between the upper and lower capacitors in the DC link.

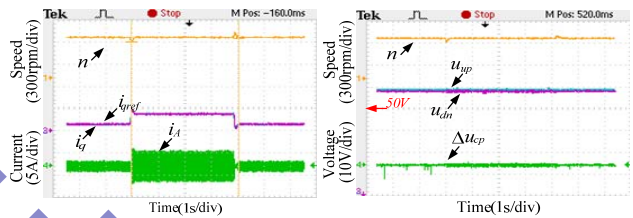

(a) (b)

Fig. 13. Measured dynamic performance of the drive of the proposed control scheme under a change in load: (a) rotor speed, q-axis current and phase A current; (b) rotor speed, DC capacitor voltages and voltage difference between the upper and lower capacitors in the DC link.

Fourthly, the measured performance of the decoupling effects of the current controller is verified as shown in Fig. 14. This verifies the validity of the feed-forward compensation for improving the dynamic performance of the drive, where the machine speed is 500 rpm. As shown in Fig. 14(a), there exists a slight disturbance in the d-axis current when the q-axis current is suddenly changed without the decoupling control. On the other hand, the d-axis and q-axis currents are decoupled well in Fig.14 (b) by adopting the decoupling control in the proposed control scheme.

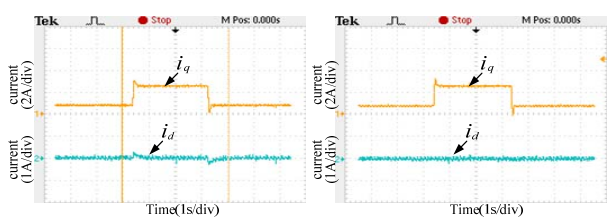

(a) (b)

Fig. 14. Measured performance of the feed-forward compensation: (a) *d-q* axis current responses without the decoupling control; (b) *d-q* axis current responses with the decoupling control.

Finally, Fig. 15 shows experiments based on NPC-3L six-phase inverter fed *RL* loads to verify the correctness of the numerical fitting surface in Fig. 6. For showing the effects of the balancing factor and modulation depth, the loading current and *pf* are kept constant at 2.42 A (rms) and 0.8, respectively. The DC link capacitor value is 2000 uF. Thus, the per unit values of the load current and DC link capacitor are I_{pu}=0.3422 and C_{pu}=2. As shown in Fig. 15(a) and Fig. 15(b), the modulation depth M is 0.75, and the values of λ are 0.5 and 1.0, respectively. The values of Δu_c are around 0.6V and 0.65V. Using the equation $z(\mathrm{V}) = \Delta u_c C_{pu} / I_{pu}$, the values of z(V) can be calculated as 3.51 and 3.80, respectively. These values agree with the corresponding values in Fig.6 (f). Similarly, when M is 1.0, and the values of λ are 0.5 and 1.0 in Fig. 15(c) and Fig. 15(d), the values of z(V) are calculated at around 7.10 and 7.60, respectively. These values are also approximately equal to the corresponding values in Fig. 6(f). In addition, Fig. 15(c) and Fig. 15(d) also verify the aforementioned conclusion that the balancing factor λ has less controllability in terms of mid-point voltage in the DC link for a high value of M.

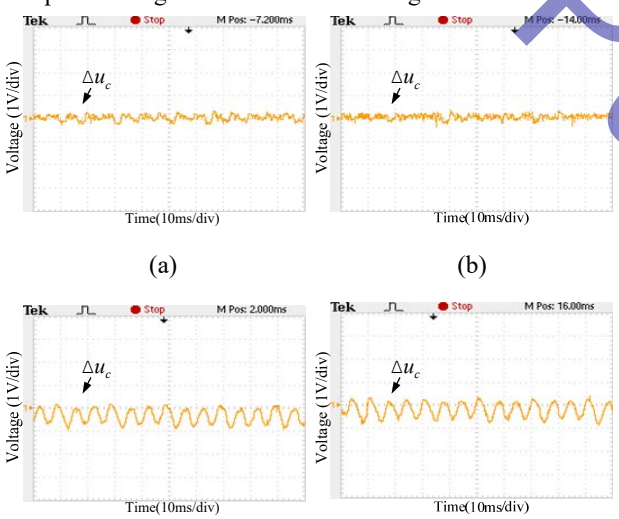

Fig. 15. Measured voltage difference between the upper and lower capacitors with *pf*=0.8: (a) M=0.75 and λ=0.5; (b) M=0.75 and λ=1.0; (b) M=1.0 and λ=0.5; and (b) M=1.0 and λ=1.0.

VII. Conclusions

This paper has studied the modelling, modulation strategy and control scheme for NPC-3L inverter fed dual three-phase PMSM drives. The key is to deduce the VSD models of the dual three-phase PMSM with asymmetric factors, and to design the DT-SVM strategy for the NPC-3L inverter. Then the control scheme is proposed for drives based on the VSD models and the DT-SVM strategy. According to the control scheme, the torque component is controlled in the *d-q* subspace, and the unbalanced currents are suppressed to zero in the *x-y* subspace by using the PRs control. The upper and lower capacitor voltages in the DC link are balanced well during various operation conditions by selecting an appropriate balancing factor with the DT-SVM. Experiments on a laboratory setup have been presented to demonstrate the validity of the proposed control scheme for NPC-3L inverter fed dual three-phase PMSM drives.

Acknowledgment

This work was supported in part by the National Key Basic Research Program of China (973 program) under Grant 2013CB035603, and in part by National Natural Science Foundation of China under Grant 51577027, and in part by the Fundamental Research Funds for the Central Universities.

References

[1] T. M. Jahns, "Improved reliability in solid-state AC drives by means of multiple independent phase-drive units," *IEEE Trans. Ind. Appl.*, Vol. 16, No. 3, pp. 321-331, May 1980.

[2] A. R. Munoz, "Dual stator winding induction machine drive," *IEEE Trans. Ind. Appl.*, Vol. 36, No. 5, pp. 1369-1379, Sep./Oct. 2000.

[3] E. Levi, R. Bojoi, F. Profumo, H. A. Toliyat and S. Williamson, "Multiphase induction motor drives - a technology status review," *IET Electric Power Appl.*, Vol. 1, No. 4, pp. 489-516, Jul. 2007.

[4] X. Wang, Z. Wang, M. Cheng, and Y. Hu "Remedial strategies of T-NPC three-level asymmetric six-phase PMSM drives based on SVM-DTC," *IEEE Trans. Ind. Electron.*, Vol. 64, No. 9, pp. 6841-6853, September 2017.

[5] L. Alberti and N. Bianchi, "Experimental Tests of Dual Three-Phase Induction Motor Under Faulty Operating Condition," *IEEE Trans. Ind. Electron.*, Vol. 59, No. 5, pp. 2041-2048, May 2012.

[6] R. H. Nelson and P. C. Krause, "Induction Machine Analysis for Arbitrary Displacement Between Multiple Winding Sets," *IEEE Trans. Power Apparatus and Systems*, Vol. PAS-93, No. 3, pp. 841-848, May 1974.

[7] M. A. Abbas, R. Christen and T. M. Jahns, "Six-Phase Voltage Source Inverter Driven Induction Motor," *IEEE Trans. Ind. Appl.*, Vol. IA-20, No. 5, pp. 1251-1259, Sep. 1984.

[8] R. Bojoi, M. Lazzari, F. Profumo and A. Tenconi, "Digital field-oriented control for dual three-phase induction motor drives," *IEEE Trans. Ind. Appl.*, Vol. 39, No. 3, pp. 752-760, May/Jun. 2003.

[9] F. Yuan, S. Huang, "A hybrid current controller for dual three-phase permanent magnet synchronous motors," *IEEJ Transactions on Electrical and Electronic Engineering*, Vol. 9 No. 2, pp. 214-218, Jan. 2014.

[10] Y. Zhao and T. A. Lipo, "Space vector PWM control of dual three-phase induction machine using vector space decomposition," *IEEE Trans. Ind. Appl.*, Vol. 31, No. 5, pp. 1100-1109, Sep./Oct. 1995.

[11] R. Bojoi, E. Levi, F. Farina, A. Tenconi and F. Profumo, "Dual three-phase induction motor drive with digital current control in the stationary reference frame," *IEE Proceedings - Electric Power Applications,* Vol. 153, No. 1, pp. 129-139, Jan. 2006.
[12] J. Karttunen, S. Kallio, P. Peltoniemi, P. Silventoinen and O. Pyrhönen, "Decoupled Vector Control Scheme for Dual Three-Phase Permanent Magnet Synchronous Machines," *IEEE Trans. Ind. Electron.*, Vol. 61, No. 5, pp. 2185-2196, May 2014.
[13] H. S. Che, E. Levi, M. Jones, W. P. Hew and N. A. Rahim, "Current Control Methods for an Asymmetrical Six-Phase Induction Motor Drive," *IEEE Trans. Power Electron.*, Vol. 29, No. 1, pp. 407-417, Jan. 2014.
[14] Y. Hu, Z. Q. Zhu and K. Liu, "Current Control for Dual Three-Phase Permanent Magnet Synchronous Motors Accounting for Current Unbalance and Harmonics," *IEEE Journal of Emerging and Selected Topics in Power Electronics,* Vol. 2, No. 2, pp. 272-284, Jun. 2014.
[15] R. Bojoi, F. Farina, G. Griva, F. Profumo and A. Tenconi, "Direct torque control for dual three-phase induction motor drives," *IEEE Trans. Ind. Appl.*, Vol. 41, No. 6, pp. 1627-1636, Nov./Dec. 2005.
[16] K. Hatua and V. T. Ranganathan, "Direct torque control schemes for split-phase induction machine," *IEEE Trans. Ind. Appl.* Vol. 41, No. 5, pp. 1243-1254, Sept./Oct. 2005.
[17] K. D. Hoang, Y. Ren, Z. Q. Zhu and M. Foster, "Modified switching-table strategy for reduction of current harmonics in direct torque controlled dual-three-phase permanent magnet synchronous machine drives," *IET Electric Power Applications*, Vol. 9, No. 1, pp. 10-19, Jan. 2015.
[18] F. Barrero, M. R. Arahal, R. Gregor, S. Toral and M. J. Duran, "One-Step Modulation Predictive Current Control Method for the Asymmetrical Dual Three-Phase Induction Machine," *IEEE Trans. Ind. Electron.*, Vol. 56, No. 6, pp. 1974-1983, Jun. 2009.
[19] M. J. Duran, J. Prieto, F. Barrero and S. Toral, "Predictive Current Control of Dual Three-Phase Drives Using Restrained Search Techniques," *IEEE Trans. Ind. Electron.*, Vol. 58, No. 8, pp. 3253-3263, Aug. 2011.
[20] R. Gregor et al., "Predictive-space vector PWM current control method for asymmetrical dual three-phase induction motor drives," *IET Electric Power Applications*, Vol. 4, No. 1, pp. 26-34, Jan. 2010.
[21] S. Kouro et al., "Recent Advances and Industrial Applications of Multilevel Converters," *IEEE Trans. Ind. Electron.*, Vol. 57, No. 8, pp. 2553-2580, Aug. 2010.
[22] A. Nabae, I. Takahashi and H. Akagi, "A New Neutral-Point-Clamped PWM Inverter," *IEEE Trans. Ind. Appl.*, Vol. IA-17, No. 5, pp. 518-523, Sep. 1981.
[23] L. Gao and J. E. Fletcher, "A Space Vector Switching Strategy for Three-Level Five-Phase Inverter Drives," *IEEE Trans. Ind. Electron.*, Vol. 57, No. 7, pp. 2332-2343, Jul. 2010.
[24] O. Dordevic, M. Jones and E. Levi, "A Comparison of Carrier-Based and Space Vector PWM Techniques for Three-Level Five-Phase Voltage Source Inverters," *IEEE Trans. Ind. Inform.*, Vol. 9, No. 2, pp. 609-619, May 2013.
[25] O. Dordevic, E. Levi and M. Jones, "A Vector Space Decomposition Based Space Vector PWM Algorithm for a Three-Level Seven-Phase Voltage Source Inverter," *IEEE Trans. Power Electron.* , Vol. 28, No. 2, pp. 637-649, Feb. 2013.
[26] H. Ryu, J. Kim and S. Sul, "Synchronous-frame current control of multiphase synchronous motor under asymmetric fault condition due to open phases," IEEE Trans. Ind. Appl. Vol. 42, No. 4, pp. 1062-1070, Jul./Aug. 2006.
[27] R. Bojoi, F. Farina, M. Lazzari, F. Profumo and A. Tenconi, "Analysis of the asymmetrical operation of dual three-phase induction machines," *in Electric Machines and Drives Conference*, pp. 429-435, Madison, Jun. 2003.
[28] N. Celanovic and D. Boroyevich, "A comprehensive study of neutral-point voltage balancing problem in three-level neutral-point-clamped voltage source PWM inverters," *IEEE Trans. Power Electron.*, Vol. 15, No. 2, pp. 242-249, Mar. 2000.
[29] B. Zhang, Z. Wang, K. Chu and M. Cheng, "Analysis of fluctuation in DC link capacitor voltage of NPC three-level inverter and its mitigation under fault tolerant control mode," *Transactions of China Electro Technical Society.*, vol. 30, no. 7, pp. 52-61, Apr. 2015.

Jian Chen received his B.S. degree from Anhui University of Science and Technology, Huainan, China, in 2013; and his M.S. degree from Southeast University, Nanjing, China, in 2016, all in Electrical Engineering. He is an Electrical Engineer with the Shenzhen Inovance Technology Co., LTD., China, where he is presently working on the R&D of low voltage drive systems.

Zheng Wang (S'05–M'09-SM'14) received his B.S. and M.S. degrees from Southeast University, Nanjing, China, in 2000 and 2003, respectively; and his Ph.D. degree from University of Hong Kong, Hong Kong, China, in 2008, all in Electrical Engineering. From 2008 to 2009, he was a Postdoctoral Fellow at Ryerson University, Toronto, ON, Canada. He is presently working as a full Professor in the School of Electrical Engineering, Southeast University. His current research interests include electric drives, power electronics, and distributed generation. He has authored or coauthored over 80 internationally refereed papers and four books in these areas. Professor Wang has received several academic awards including an IEEE PES Chapter Outstanding Engineer Award, a Best Paper Award of the International Conference on Electrical Machines and Systems (ICMES), a Best Session Paper Award of the IEEE Annual Meeting of Industrial Electronics (IECON), and a Nanjing Outstanding Paper Award of Natural Science.

Yibo Wang received his B.S. degree in Electrical Engineering from Southeast University, Nanjing, China, in 2015, where he is presently working towards his M.S. degree. His current research interests include multilevel converters, multilevel PWM strategies, the control of multiphase permanent magnet synchronous motors, and the fault tolerant control of multiphase motors.

Ming Cheng (M'01–SM'02-F'15) received his B.S. and M.S. degrees from

the Department of Electrical Engineering, Southeast University, Nanjing, China, in 1982 and 1987, respectively; and his Ph.D. degree from the Department of Electrical and Electronic Engineering, University of Hong Kong, Hong Kong, China, in 2001, all in Electrical Engineering. Since 1987, he has been with Southeast University, where he is presently working as a Distinguished Professor in the School of Electrical Engineering and as the Director of the Research Center for Wind Power Generation. From January to April 2011, he was a Visiting Professor in the Wisconsin Electric Machine and Power Electronics Consortium, University of Wisconsin, Madison, WI, USA. His current teaching and research interests include electrical machines, motor drives for EVs, and renewable energy generation. He has authored or co-authored more than 300 technical papers and four books, and is the holder of 70 patents in these areas. Professor Cheng is a Fellow of the Institution of Engineering and Technology. He has served as a Chair and as an Organizing Committee Member for many international conferences. He was a Distinguished Lecturer of the IEEE Industry Applications Society in 2015/2016.